RSC Advances

ROYAL SOCIETY OF CHEMISTRY

PAPER

View Article Online
View Journal | View Issue

Cite this: *RSC Adv.*, 2026, **16**, 8601

In situ generation of hydrogen peroxide using a schwertmannite/nickel foam catalyst for enhanced heterogenous Fenton degradation of dye wastewater

Kun Feng,[a] Shuping Zhang,[a] Yanni Liu,[b] Yongjun Shen,[a] Pin Zhou,[a] Jiayu Gu,[a] Mingjie Yin[a] and Neng Tao *[a]

Conventional Fenton processes face challenges such as the need for external hydrogen peroxide (H_2O_2) addition, leading to low oxidant utilization efficiency, high costs, and safety risks. To address these limitations, a novel heterogeneous Fenton catalyst was fabricated by supporting schwertmannite (Sch) on nickel foam (NF) for the degradation of Rhodamine B (RhB). This system enables the *in situ* generation of H_2O_2 through an oxygen reduction reaction (ORR) pathway on the NF substrate. Under optimized conditions (20 mg L^{-1} RhB, pH 2.0, 180 rpm), the Sch/NF composite achieved 99% RhB decolorization within 15 min. Quenching experiments and electron paramagnetic resonance analyses identified hydroxyl radicals ($^{\bullet}OH$) and singlet oxygen ($^1O_2$) as the dominant reactive species. The enhanced catalytic performance is attributed to the accelerated Fe^{2+}/Fe^{3+} cycling, facilitated by electron donation from the Ni/Ni^{2+} redox couple within the NF support. This synergy enables the continuous regeneration of Fe^{2+} sites, which subsequently activate the *in situ* generated H_2O_2 to produce radicals. This work provides a feasible strategy for constructing high-performance, self-sustaining heterogeneous Fenton catalysts for efficient dye wastewater treatment.

Received 11th December 2025
Accepted 3rd February 2026

DOI: 10.1039/d5ra09613h

rsc.li/rsc-advances

1. Introduction

The persistent discharge of synthetic dyes into aquatic ecosystems poses significant environmental and health risks due to their inherent toxicity, carcinogenicity, and resistance to natural degradation.[1,2] This concern is particularly evident for Rhodamine B (RhB), a stable xanthene-based dye widely used in textile manufacturing and biomedical applications.[3,4] Conventional wastewater treatment methods, such as adsorption and biological processes, often fail to achieve complete mineralization, frequently resulting in secondary pollution or requiring energy-intensive post-treatment steps.[2] Consequently, developing advanced treatment technologies for textile effluents is imperative for effective detoxification and compliance with stringent environmental regulations.

Advanced oxidation processes (AOPs), particularly Fenton-based systems, have emerged as promising alternatives for degrading refractory organic pollutants through the *in situ* generation of reactive oxygen species (ROS).[5,6] Heterogeneous Fenton catalysts are considered superior to their homogeneous counterparts, as they operate over a broader pH range, reduce sludge production, and improve the utilization efficiency of hydrogen peroxide (H_2O_2).[7,8] Nevertheless, the reliance on continuous external H_2O_2 addition remains a fundamental limitation, increasing operational complexity and costs. Therefore, exploring efficient Fenton systems with *in situ* H_2O_2 generation capability is of great interest.

Schwertmannite ($Fe_8O_8(OH)_{8-2x}(SO_4)_x \cdot nH_2O$, $1.0 \leq X \leq 1.75$, Sch), a naturally occurring Fe(III)-oxyhydroxysulfate mineral, exhibits considerable potential as a heterogeneous Fenton catalyst.[9,10] Its high specific surface area, acid-buffering capacity, and intrinsic sulfate and hydroxyl groups facilitate efficient ROS generation *via* both hydroxyl radical ($^{\bullet}OH$) and sulfate radical pathways.[11,12] To enhance the catalytic performance of Sch and mitigate its particle agglomeration, three-dimensional porous materials and semiconductor supports have been employed to promote Fe^{2+} regeneration.[6,13] However, the practical application of Sch is hindered by intrinsic limitations, including sluggish Fe^{3+}/Fe^{2+} redox cycling, structural instability, and challenges in recovery.[13,14]

Nickel foam (NF) has gained attention as an efficient scaffold due to its three-dimensional macroporous structure, excellent electrical conductivity, and favorable magnetic properties.[15] These characteristics facilitate the anchoring of nanomaterials and enhance catalytic performance in pollutant

[a]*Research Center of Secondary Resources and Environment, School of Chemical Engineering and Materials, Changzhou Institute of Technology, Changzhou 213022, China. E-mail: SZHCH99@163.com*

[b]*Shandong Wandou Inspection Services Co., Ltd, Weifang 261205, China*

degradation.[15–18] Moreover, NF can activate molecular oxygen (O_2) to generate H_2O_2 *in situ* and promote the redox cycling between Fe^{3+} and Fe^{2+} in Fenton-like systems.[19] Based on these attributes, we hypothesized that constructing a composite catalyst through the *in situ* growth of Sch on an NF substrate (Sch/NF) would yield synergistic effects, including: (i) the *in situ* supply of H_2O_2 *via* NF-mediated O_2 activation; (ii) accelerated reduction of Fe^{3+} to Fe^{2+} facilitated by electron transfer from NF; and (iii) facile magnetic separation of the catalyst.

This study reports the synthesis of a novel Sch/NF composite catalyst. The specific objectives were to: (I) evaluate its catalytic performance for RhB degradation; (II) investigate the influence of different factors such as pH, RhB concentration, rotation rate, and quantify *in situ* H_2O_2 production; (III) identify the dominant reactive species; and (IV) elucidate the mechanism. This work aims to develop an efficient, self-sustaining material for advanced wastewater treatment.

2. Experimental

2.1 Chemicals and reagents

Ferrous sulfate heptahydrate ($FeSO_4 \cdot 7H_2O$, AR grade), hydrogen peroxide (H_2O_2, 30%, w/w), sodium hydroxide (NaOH, AR grade), sulfuric acid (H_2SO_4, AR grade), and RhB (AR grade) were purchased from Sinopharm Chemical Reagent Co., Ltd. NF, potassium titanium oxalate (AR grade), 5,5-dimethyl-1-pyrroline-*N*-oxide (DMPO, AR grade), and 2,2,6,6-tetramethylpiperidine (TEMP, AR grade) were obtained from Macklin Biochemical Co., Ltd. Deionized water was used throughout all experiments.

2.2 Preparation of catalyst

The Sch/NF composite was synthesized following a previously reported method with minor modifications.[9] Briefly, a piece of NF (3×3 cm^2) was ultrasonically cleaned sequentially with 5% HCl, ethanol (75%), and deionized water for 30 min to remove surface impurities and oxides, followed by vacuum drying at 60 °C.[18] Subsequently, five pieces of the pre-treated NF were immersed in a 500 mL triangular flask containing 250 mL of a 160 mM $FeSO_4 \cdot 7H_2O$ solution (pH = 2.5). Then, 6 mL of a 9.97 mM H_2O_2 was added to the solution. The mixture was allowed to react for 24 h at 28 °C under continuous shaking at 180 rpm. The resulting Sch/NF composite, along with any precipitated Sch, was collected, thoroughly rinsed with acidified deionized water (pH = 2), and dried at 60 °C until a constant weight. The Sch loading on the NF was determined to be approximately 1.6 g m^{-2} by measuring the weight difference of the NF before and after synthesis.

2.3 Experimental procedures

The RhB degradation experiments were conducted in 100 mL triangular flasks. Typically, one piece of pristine NF or the as-prepared Sch/NF catalyst was added to 50 mL of an RhB solution (20 mg L^{-1}). The initial pH of the solution was adjusted using 0.05 M NaOH or 0.05 M H_2SO_4. The reaction was initiated by placing the flasks in a rotary shaker maintained at 25 °C and 180 rpm. At predetermined time intervals, 2 mL aliquots of the reaction mixture were withdrawn and immediately filtered through a 0.45 μm membrane filter for subsequent analysis.

2.4 Analytical methods

The morphology and elemental composition of the catalysts were characterized by scanning electron microscopy (SEM, Hitachi, Japan) coupled with an energy-dispersive X-ray spectrometer (EDS). Crystal structures were analyzed using X-ray powder diffraction (XRD) with Cu Kα radiation (30 kV, 15 mA). Functional groups were identified by Fourier-transform infrared spectroscopy (FTIR) on a Nicolet IS10 spectrometer (USA) using KBr pellets. The surface chemical states were analyzed by X-ray photoelectron spectroscopy (XPS) on a Thermo Scientific ESCALAB 250Xi system with Al Kα radiation. The concentration of RhB was monitored using a UV-2202pc ultraviolet-visible (UV-vis) spectrophotometer. The concentration of Fe^{2+} was determined by the 1,10-phenanthroline method. The H_2O_2 concentration was measured *via* colorimetric titration using titanium potassium oxalate. Active radical species were identified using a JES-FA200 electron paramagnetic resonance (EPR) spectrometer with DMPO and TEMP as spin-trapping agents. Furthermore, quenching experiments were conducted using methanol (88 mM, a potent $^{\cdot}OH$ scavenger), furfuryl alcohol (FFA, 10 mM, a selective $^1O_2$ scavenger), and potassium dihydrogen phosphate (KH_2PO_4, 1 mM, which complexes with dissolved Fe ions and may passivate surface sites) to identify the dominant reactive species.[20,21]

3. Results and discussion

3.1 Characterization

The morphology and composition of the synthesized materials were examined using SEM coupled with EDS. As shown in Fig. 1, the pristine NF exhibited a three-dimensional network of smooth fibers. In contrast, the surface of the NF in the Sch/NF composite was covered with a dense layer. Higher-magnification images revealed that the deposited Sch particles were significantly agglomerated, with an average size of approximately 500 nm (Fig. S1). The typical sea urchin-like morphology of Sch was not observed. This is likely due to the rapid oxidation and precipitation induced by the single-batch addition of H_2O_2, which inhibited oriented crystal growth.[9,10] EDS elemental mapping (Fig. S7a) confirmed the uniform distribution of Fe (14.06%), O (12.67%) and S (1.90%) across the NF surface with relative atomic weight percentage, co-localizing with Ni (71.38%), providing direct evidence for the successful loading of Sch.

The XRD pattern of the precipitate collected from the synthesis solution matched the reference pattern for Sch (JCPDS 47-1775), showing characteristic peaks at 26.2°, 35.1°, 55.3° and 61.3° (Fig. 2a).[22] For the Sch/NF composite, the XRD pattern was dominated by intense peaks from the metallic Ni phase (JCPDS 04-0850). The absence of distinct Sch peaks is attributed to the strong diffraction signal from the highly crystalline NF, the relatively low Sch loading, and its inherent poor crystallinity. As

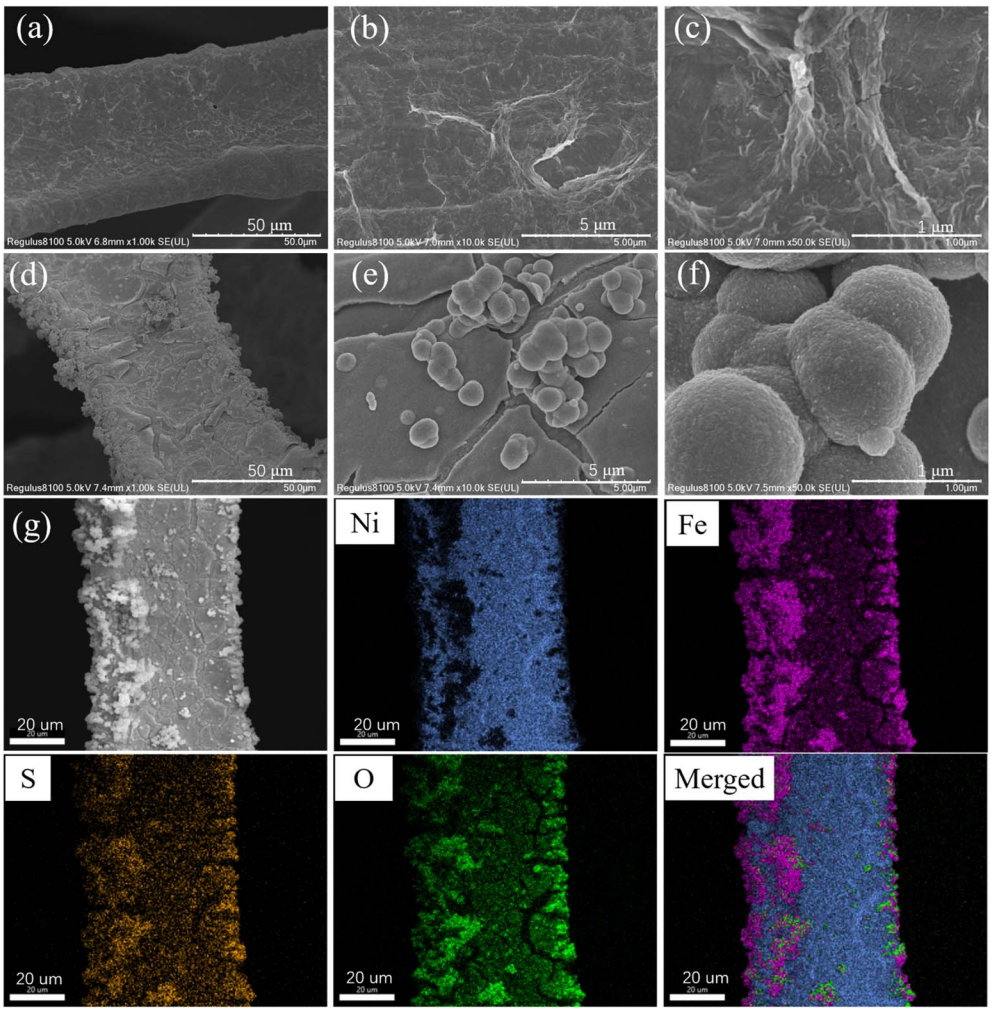

Fig. 1 SEM images of the NF (a–c) and obtained Sch/NF catalyst (d–f). SEM and EDS elemental mapping of Ni, Fe, S, and O elements recoded from Sch/NF catalyst (g).

observed in composites such as Fe_3O_4/Sch and WS_2@Sch, the sharp diffraction peaks of the well-crystalline phases (Fe_3O_4 or WS_2) dominate the XRD patterns, while the characteristic reflections of Sch are either overshadowed or undetectable due to its inherent poor crystallinity.[21,23] FTIR spectroscopy (Fig. 2b) provided further evidence for Sch incorporation with both Sch and Sch/NF samples showing a characteristic absorption peak at 1128 cm^{-1}, attributed to SO_4^{2-} stretching vibrations.[22]

XPS analysis was employed to investigate the surface chemical states. The survey spectrum (Fig. S2a) confirmed the presence of Ni 2p, Fe 2p, S 2p and O 1s. The high-resolution Fe 2p spectrum of pure Sch sample exhibited Fe $2p_{3/2}$ peaks at binding energies of 711.2 eV and 713.1 eV, attributed to Fe^{2+} and Fe^{3+} species, respectively (Fig. S2b). In the fresh Sch/NF composite, these peaks shifted to lower binding energies (710.9 eV and 712.9 eV, respectively), indicating a change in the chemical environment of Fe, likely due to electron transfer from the NF substrate (Fig. 2c). The surface molar ratio of Fe^{2+} to Fe^{3+} in the Sch/NF was 1.5, markedly higher than the ratio of 0.8 in pure Sch. This suggests that the NF substrate facilitated the reduction of Fe^{3+} to Fe^{2+} during synthesis. The high-resolution Ni2p spectrum of Sch/NF composite (Fig. 2d) showed peaks at 853.6 eV and 871.0 eV were assigned to Ni^{2+}, while those at 856.3 eV and 873.6 eV were characteristic of Ni^{3+}, along with their satellite peaks.[17] The presence of oxidized Ni species indicates surface oxidation of the NF during synthesis, consistent with its role as an electron donor.[19] The initial surface molar ratio of Ni^{2+} to Ni^{3+} was 0.12.

3.2 Catalytic performance and H_2O_2 production

The catalytic performance of the Sch/NF was evaluated through RhB degradation (Fig. 3a). Control experiments confirmed RhB stability at pH = 2 without a catalyst. Pristine NF alone achieved 69% RhB removal in 30 min, likely due to its ability to activate dissolved oxygen, generating $^{\cdot}O_2^-$ and subsequently H_2O_2, which can contribute to oxidation.[19] The Sch/NF composite demonstrated significantly enhanced activity, removing 99% of RhB within 15 min, compared to 42% for pure NF at the same time point. This synergy indicates that the integration of Sch with NF promotes efficient ROS generation.

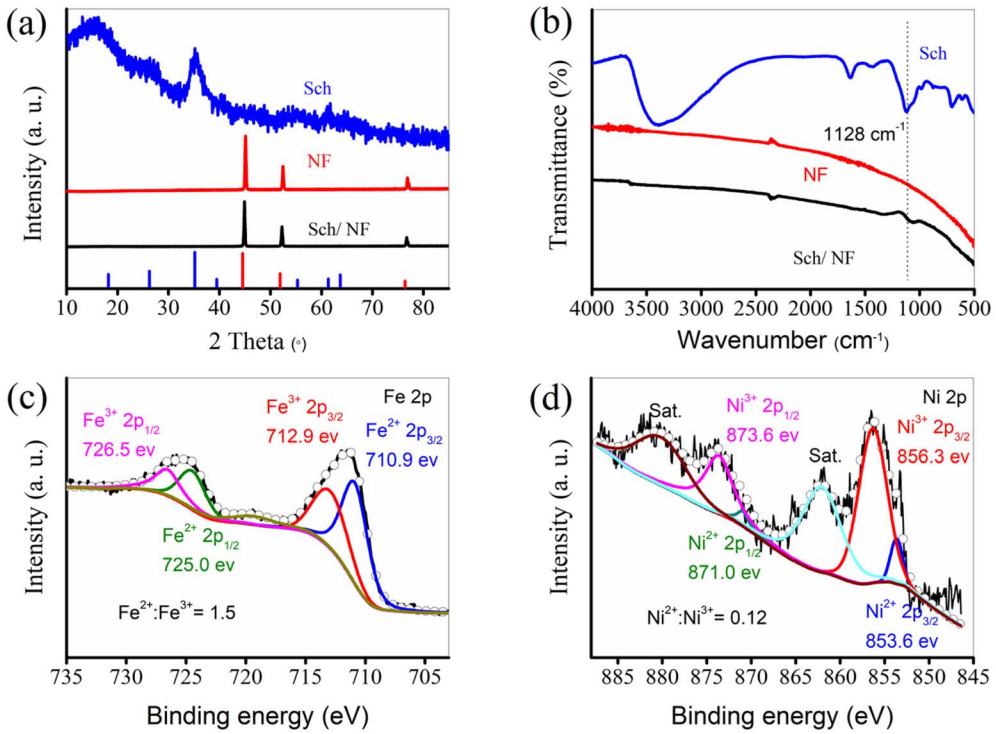

Fig. 2 XRD patterns (a) and FTIR (b) of NF, Sch/NF and obtained Sch (b).High resolution X-ray photoelectron spectroscopy (XPS) of Fe 2p (c) and Ni 2p (d) for the Sch/NF. The red and blue lines correspond to the standard XRD patterns of NF (JCPD 04-0850) and Sch (JCPD 47-1775) at the bottom of the figure (a).

The effect of initial solution pH on the degradation efficiency was shown in Fig. 3b. The Sch/NF system exhibited high activity under acidic conditions (pH < 4). Within the pH range of 3.0 to 2.0, the removal efficiency increased from 85% to 99% within 15 min. The enhanced performance under acidic conditions can be attributed to multiple factors, including the improved

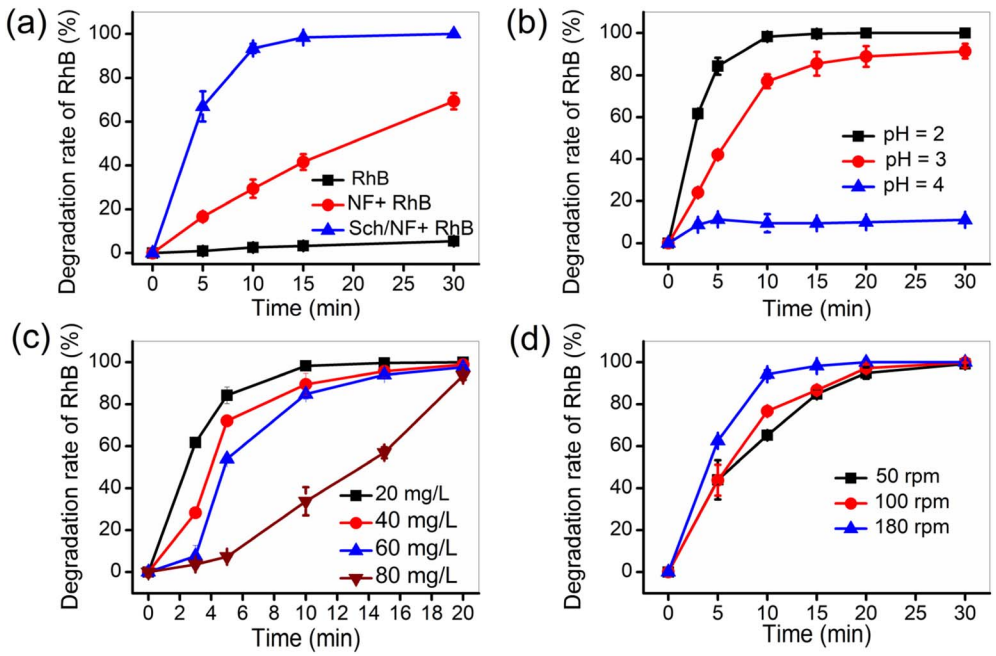

Fig. 3 Catalytic activity of Sch/NF catalyst for RhB degradation. RhB: 20 mg L^{-1}, a piece of Sch/NF (3 cm * 3 cm), pH = 2, rotation rate: 180 rpm. (a) RhB degradation efficiency in various reaction systems. (b) Effect of initial pH on RhB degradation by Sch/NF reaction. (c) Variation of RhB concentration in solution plotted with reaction time during Sch/NF reaction. (d) The effect of rotation rate on RhB degradation by Sch/NF reaction.

stability of Sch, the potential dissolution of nickel ions, and a more favorable environment for ˙OH generation *via* the Fenton-like reaction.[6,24] The influence of initial RhB concentration was also investigated (Fig. 3c). The removal efficiency within 10 min exhibited an inverse correlation with concentration (20–80 mg L^{-1}), declining from 99% at 20 mg L^{-1} to 34% at 80 mg L^{-1}. Notably, at 80 mg L^{-1}, the removal efficiency was only about one-third of that observed at lower concentrations, indicating that the catalytic capacity of Sch/NF becomes saturated at higher pollutant loads. In addition, to evaluate the broad-spectrum applicability of the Sch/NF composite, its catalytic performance was examined using three structurally distinct model pollutants: tetracycline hydrochloride, methylene blue, and aniline blue. As shown in Fig. S3, high removal efficiencies of 73%, 98%, and 94% were achieved within 15 min, respectively. These results confirm its broad-spectrum activity and potential for treating complex wastewater.

Since dissolved O_2 is the precursor for ROS, the impact of O_2 mass transfer was probed by varying the rotational speed (Fig. 3d). The degradation rate increased with rotational speed. At lower speeds (50–100 rpm), the removal efficiency within 15 min ranged from 85% to 87%. When the rotational speed was increased to 180 rpm, the degradation rate was significantly enhanced to 99%. This trend is consistent with enhanced oxygen transfer from the gas phase to the liquid–catalyst interface at higher mixing intensities, underscoring the critical role of dissolved O_2 in the degradation process. Furthermore, the effects of light irradiation and catalyst dosage were investigated (Fig. S4). The negligible effects of light irradiation and catalyst dosage suggest that the rate-limiting step in this system is likely the NF-mediated electron transfer and subsequent *in situ* H_2O_2 generation, rather than processes dependent on photon energy or the total Sch surface area.

Notably, the *in situ* production of H_2O_2 was quantitatively monitored. As illustrated in Fig. 4a, the H_2O_2 concentration in the solution phase increased gradually, reaching a maximum of 9.51 mg L^{-1} over 30 min. This represents the net accumulation of H_2O_2, implying that its generation rate exceeded its consumption rate (*via* Fenton reaction and decomposition) under the tested conditions. This measurable H_2O_2 pool confirms the successful implementation of the *in situ* generation strategy. Table S1 summarizes the performance of various catalyst systems for *in situ* production H_2O_2 and organic pollutant degradation. The data indicate that the H_2O_2 yield of Sch/NF, while higher than that of pristine graphitic carbon nitride (g-C_3N_4), is still considerably lower than that of modified g-C_3N_4. Furthermore, under typical Fenton-like reaction *in situ* production H_2O_2 conditions, the RhB removal efficiency typically ranges from 88%∼96% within 50 min.

3.3 Identification of active species

Quenching experiments and EPR spectroscopy were employed to identify the reactive species responsible for RhB degradation. FFA and methanol were applied to quench $^1O_2$ and ˙OH, respectively. Additionally, KH_2PO_4 was used to sequester dissolved Fe^{2+}/Fe^{3+} ions, thus assessing the contribution of the homogeneous Fenton reaction, although it should be noted that phosphate may also passivate surface iron sites to some extent. As shown in Fig. 5a, the addition of both FFA and methanol (˙OH quencher) strongly inhibited RhB degradation. In contrast, KH_2PO_4, which complexes free Fe^{2+}/Fe^{3+} ions, exerted a weaker inhibitory effect. These results indicated that $^1O_2$ and

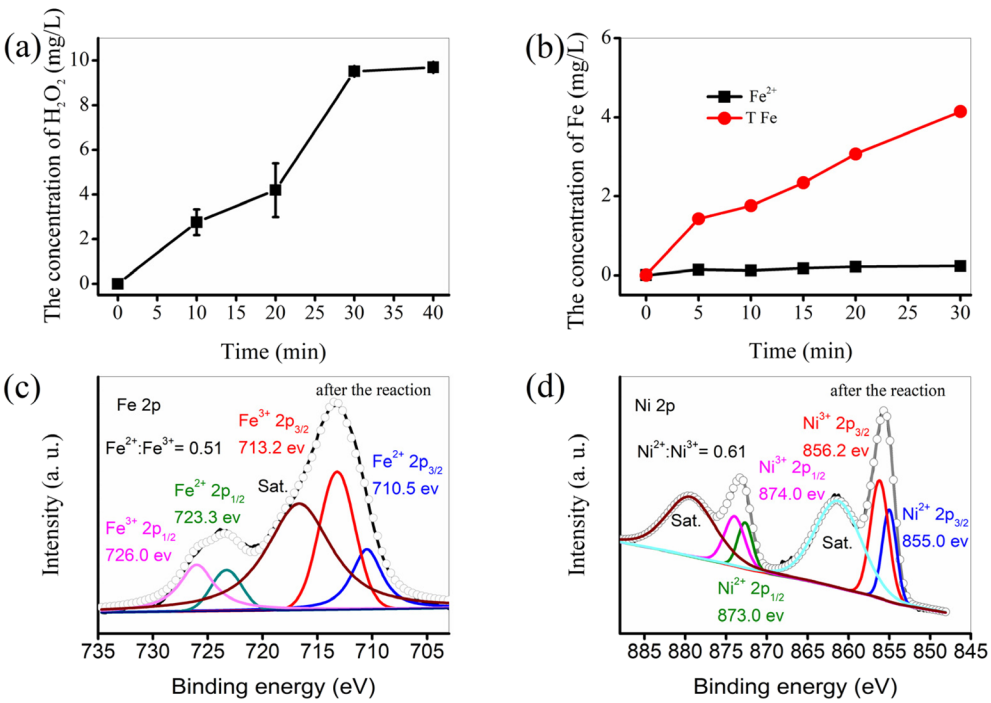

Fig. 4 Content change of H_2O_2 (a), Fe^{2+} and total Fe (TFe) (b) in the degradation of RhB by Sch/NF catalyst. XPS spectra of Fe 2p (c) and Ni 2p (d) in Sch/NF.

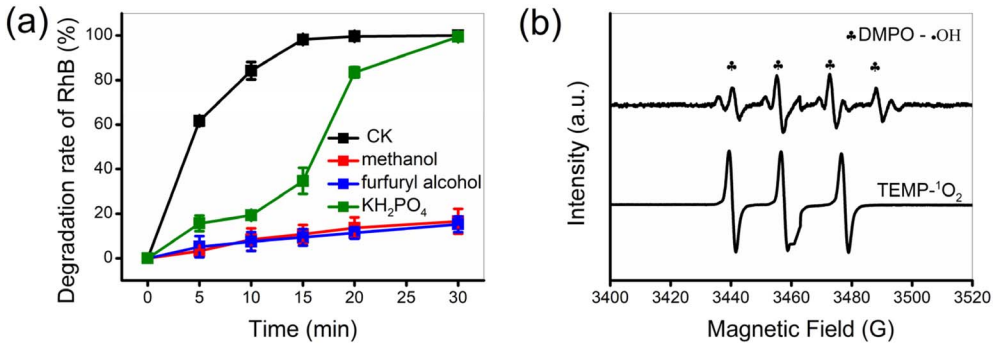

Fig. 5 (a) Effect of scavengers on RhB degradation in the Sch/NF systems. (b) ESR spectra of reactive oxygen species produced in the Sch/NF systems. Reaction conditions: pH = 2, a piece of Sch/NF (3 cm × 3 cm), RhB: 20 mg L^{-1}, rotation rate: 180 rpm.

$^{\bullet}OH$ are the primary reactive species, while the contribution from homogeneous Fenton involving leached iron ions is minor.

EPR spectroscopy with spin-trapping agents provided direct evidence for radical generation (Fig. 5b). The characteristic quartet signal of DMPO-$^{\bullet}OH$ (with a 1 : 2 : 2 : 1 intensity ratio) was detected, confirming the production of $^{\bullet}OH$. When methanol was used as the reaction solvent, no characteristic EPR signal of $^{\bullet}O_2^-$ radicals was detected, indicating that $^{\bullet}O_2^-$ is likely a transient intermediate that is rapidly converted into other reactive species in this system. Simultaneously, a three-line signal with a 1 : 1 : 1 intensity ratio was observed and assigned to TEMP-$^1O_2$ adduct. These EPR findings unequivocally demonstrate the concurrent generation of both $^{\bullet}OH$ and $^1O_2$ in the Sch/NF system.

Given its higher redox potential (~2.8 V) compared to $^1O_2$ (~2.2 V), $^{\bullet}OH$ is thermodynamically more aggressive and acts as the primary species responsible for RhB degradation. Furthermore, the detected $^1O_2$ likely forms *in situ* through follow pathways: $^{\bullet}O_2^-$ generated from O_2 activation on NF

$$Ni + 2O_2 \rightarrow Ni^{2+} + 2{}^{\bullet}O_2^- \quad (1)$$

undergo disproportionation

$$2{}^{\bullet}O_2^- + 2H_2O \rightarrow {}^1O_2 + H_2O_2 + 2OH^- \quad (2)$$

or react with $^{\bullet}OH$.[19]

$$^{\bullet}OHO_2^- + {}^{\bullet}OHOH \rightarrow {}^1O_2 + OH^- \quad (3)$$

This pathway also could account for the lack of a distinct EPR signal for the $^{\bullet}OHO_2^-$. Thus, $^{\bullet}OHOH$ plays the dominant degradative role, while $^1O_2$ is a concomitant product of these radical processes.

3.4 Proposed catalytic mechanism and redox cycling

Based on the collective evidence, a catalytic mechanism is proposed (Fig. 6). In the Sch/NF system, H_2O_2 is generated primarily through the direct two-electron oxygen reduction reaction (ORR) on the metallic nickel (Ni^0) surface, as represent by:

$$O_2 + 2H^+ + 2e^- \rightarrow H_2O_2 \quad (4)$$

Although the sequential one electron transfer *via* a $^{\bullet}OHO_2^-$ (eqn (1) to eqn (3)) intermediate is thermodynamically plausible and has been reported in prior studies,[19] it is considered

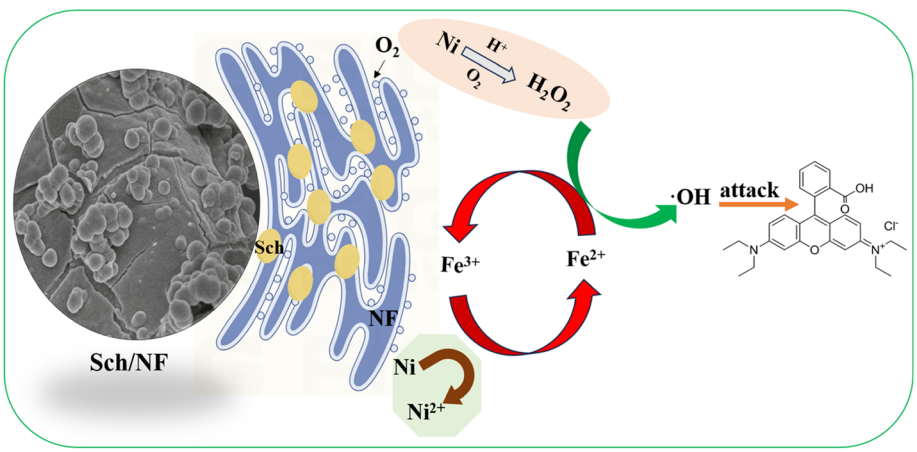

Fig. 6 Proposed mechanism for catalytic activity of Sch/NF catalyst.

a minor pathway in this system. This conclusion is supported by the efficient H_2O_2 yield and the absence of a distinct $^{\cdot}OHO_2^-$ signal in our EPR measurements.

The *in situ* generated H_2O_2, both in the solution phase and more importantly at the catalyst–liquid interface, is then activated by the $\equiv Fe^{2+}$ sites within the Sch layer to produce

$$^{\cdot}OH\ (Fe^{2+} + H_2O_2 \rightarrow Fe^{3+} + OH^- + {}^{\cdot}OHOH \quad (5)$$

which is the primary agent for RhB degradation. A key synergistic step is the rapid regeneration of $\equiv Fe^{2+}$. The spent catalyst ($\equiv Fe^{3+}$) is reduced back to its active state by electron transfer from the underlying NF (eqn (6) to eqn (8)), a process thermodynamically favored given the standard redox potentials (E^0 (Fe^{3+}/Fe^{2+}) = +0.77 V *vs.* SHE; E^0 (Ni^{2+}/Ni) = −0.25 V *vs.* SHE).

$$Ni \rightarrow Ni^{2+} + 2e^- \quad (6)$$

$$2 \equiv Fe^{3+} + 2e^- \rightarrow 2 \equiv Fe^{2+} \quad (7)$$

$$\text{Overall: } 2 \equiv Fe^{3+} + Ni \rightarrow 2 \equiv Fe^{2+} + Ni^{2+} \quad (8)$$

This electron transfer is corroborated by XPS analysis of fresh and spent catalysts. The surface $\equiv Fe^{2+}/\equiv Fe^{3+}$ ratio decreased from 1.5 in the fresh Sch/NF to 0.5 after reaction (Fig. 2c and 4c), confirming the oxidation of Fe during the Fenton process. Correspondingly, the surface Ni^{2+}/Ni^{3+} molar ratio increased from 0.1 to 0.6 (Fig. 2d and 4d), confirming the oxidation of NF and its role as an electron donor. This continuous cycle of H_2O_2 production and Fe^{2+} regeneration enables the persistent generation of ROS.

While iron leaching was observed (Fig. 4b), a control experiment using equivalent concentrations of leached Fe^{2+} (0.2 mg L^{-1}) and added H_2O_2 (10 mg L^{-1}) achieved only 12% RhB removal in 30 minutes (Fig. S5), significantly lower than the 99% removal by Sch/NF. This definitively demonstrates that the homogeneous Fenton pathway plays a negligible role, and the reaction is primarily catalyzed heterogeneously at the Sch/NF interface.

3.5 Reusability and stability of Sch/NF

The reusability and stability of Sch/NF composite were evaluated over three consecutive cycles (Fig. S6). The RhB degradation efficiency decreased markedly from 99% in the first cycle to 34% in the second and 7% in the third, indicating significant catalyst deactivation. This performance loss is contrasts with studies reporting the stability of pure Sch under different reaction conditions, highlighting the impact of the NF support and the specific reaction environment on Sch stability.[25] However, supported Sch composites, such as the WS_2@Sch system noted for methylene blue degradation, have also exhibited stability challenges.[21] In the present study, the performance decay of Sch/NF was attributed to the following interrelated factors. First, the loss of active material was a primary cause. EDS analysis (Fig. S7b) shown that after three cycles, the relative atomic percentage of Fe and S in Sch/NF composite decreased to 2.03% and 0.78%, respectively, from their initial values of 14.06% and 1.90%. The relatively low loading of Sch on the NF surface was further diminished during repeated reaction and recovery steps, directly reducing the number of available catalytic sites. Second, mineral phase transformation likely occurred. Sch is a metastable, amorphous iron oxyhydroxysulfate that can readily transform into more thermodynamically stable but less active crystalline phases (*e.g.*, goethite), under acidic and oxidizing conditions, which would significantly contribute to the activity loss. Third, surface passivation of the NF substrate may have occurred. Previous studies have shown that a non-conductive or less-reactive layer of nickel hydroxide ($Ni(OH)_2$) or nickel oxide (NiO) could form on the NF surface under acidic conditions.[26,27] SEM images (Fig. S8) also revealed a significant morphological transformation of Sch/NF composite after three cycles, from an initial spherical shape to a petal-like structure, indicating substantial surface reconstruction during the reaction. The formation of such an insulating layer would impede electron transfer from the NF core to the supported Sch, thereby hindering the regeneration of $\equiv Fe^{2+}$ sites and disrupting the synergistic catalytic cycle.

4. Conclusion

This study presents a self-sustaining heterogeneous Fenton system by immobilizing Sch on NF. The Sch/NF composite achieved efficient RhB degradation (99% within 15 min under optimal conditions), which is attributed to the synergistic dual function of the NF substrate. Specifically, NF facilitates the *in situ* generation of H_2O_2 through an ORR, while simultaneously acting as an electron donor to promote the $\equiv Fe^{3+}/\equiv Fe^{2+}$ redox cycling on Sch. This continuous regeneration of active Fe^{2+} sites enables the sustained production of $^{\cdot}OH$, identified as the dominant reactive species responsible for RhB degradation. However, the catalyst's stability requires further improvement, as its activity decreased significantly over three consecutive cycles. This decline can be attributed to several interrelated factors: the leaching and possible phase transformation of Sch under reaction conditions, along with surface passivation of the NF support, which collectively hinder electron transfer and long-term catalytic performance. Despite these current limitations, this work demonstrates a viable strategy for constructing *in situ* H_2O_2 driven Fenton systems using three dimensional supports. Future research should aim to enhance interfacial stability through approaches such as strengthening the Sch/NF interaction, structural doping of Sch, or exploring more robust support materials, thereby advancing the practical application of such self-sustaining catalysts in wastewater treatment.

Author contributions

Kun Feng: conceptualization, writing – original draft, formal analysis, funding acquisition, Shuping Zhang: data curation, methodology, Yanni Liu: investigation, Yongjun Shen: supervision, Jiayu Gu: methodology, Pin Zhou: resources, supervision, Mingjie Yin: investigation, methodology, Neng Tao: supervision, writing – review, funding acquisition.

Conflicts of interest

There are no conflicts to declare.

Data availability

The data will be made available from the corresponding author upon reasonable request.

Supplementary information (SI) is available. See DOI: https://doi.org/10.1039/d5ra09613h.

Acknowledgements

This work was supported by the National Natural Science Foundation of China (No. 52300148) and the Changzhou Science and Technology Plan Applied Basic Research Project (No. CJ20235076).

References

1 M. S. Kumar, S. H. Sonawane and A. B. Pandit, *Chem. Eng. Process. Process Intensif.*, 2017, **122**, 288–295.
2 T. de Oliveira Guidolin, N. M. Possolli, M. B. Polla, T. B. Wermuth, T. F. de Oliveira, S. Eller, O. R. K. Montedo, S. Arcaro and M. A. P. Cechinel, *J. Cleaner Prod.*, 2021, **318**, 128556.
3 S. Manna, D. Roy, P. Saha, D. Gopakumar and S. Thomas, *Process Saf. Environ. Prot.*, 2017, **107**, 346–356.
4 M. R. Ladole, P. B. Pokale, S. S. Patil, P. G. Belokar and A. B. Pandit, *Bioresour. Technol.*, 2020, 124035.
5 N. Barhoumi, N. Oturan, H. Olvera-Vargas, E. Brillas, A. Gadri, S. Ammar and M. A. Oturan, *Water Res.*, 2016, **94**, 52–61.
6 X. X. Qiao, X. J. Liu, W. Y. Zhang, Y. L. Cai, Z. Zhong, Y. F. Li and J. Lü, *Sep. Purif. Technol.*, 2021, 119760.
7 E. Neyens and J. Baeyens, *J. Hazard. Mater.*, 2003, **98**, 33–50.
8 N. Wang, T. Zheng, G. Zhang and P. Wang, *J. Environ. Chem. Eng.*, 2016, **4**, 762–787.
9 F. Liu, J. Zhou, S. Zhang, L. Liu, L. Zhou and W. Fan, *PLoS One*, 2015, **10**, 0138891.
10 K. Feng, X. Wang, B. Ding, M. Xu, J. Liang and L. Zhou, *Chem. Geol.*, 2022, 120828.
11 S. Yan, L. Zhan, X. Meng, D. Wang, X. Wang, G. Zheng, J. Lu and L. Zhou, *Sep. Purif. Technol.*, 2021, 118991.
12 T. Li, Y. Chen, X. Wang, J. Liang and L. Zhou, *Appl. Catal., B*, 2020, 119830.
13 X. Wang, L. Dai, S. He, Y. Wang and Y. Zhang, *Sep. Purif. Technol.*, 2023, 123314.
14 Z. Yang, P. Zhu, C. Yan, D. Wang, D. Fang and L. Zhou, *Chemosphere*, 2020, 129175.
15 J. Wang, M. Wang, J. Kang, Y. Tang, Z. Xu, Q. Dong, T. Ma and J. Zhu, *Sep. Purif. Technol.*, 2023, 123584.
16 X. Chen, T. Zhang, M. Kan, D. Song, J. Jia, Y. Zhao and X. Qian, *Environ. Sci. Technol.*, 2020, **54**, 13344–13353.
17 Y. Yao, W. Wang, H. Hu, L. Zhang, Z. Ma and S. Wang, *Chem. Eng. Sci.*, 2024, **297**, 120276.
18 Y. Yao, Z. Tao, H. Hu, L. Zhang, Z. Ma, Y. Wang, S. Lin and S. Wang, *J. Environ. Sci.*, 2025, **150**, 704–718.
19 W. Wan, Y. Zhang, R. Ji, B. Wang and F. He, *ACS Omega*, 2017, **2**, 6104–6111.
20 L. Liu, D. Guo, G. Qiu, C. Liu and Z. Ning, *J. Environ. Manage.*, 2022, **317**, 115425.
21 K. Feng, S. Zhang, N. Tao, Z. Sun, X. Kong, Y. Tan, X. Liu, L. Zhou, P. Zhou and Y. Shen, *J. Environ. Sci.*, 2025, **163**, 126–135.
22 Z. Zhang, X. Bi, X. Li, Q. Zhao and H. Chen, *RSC Adv.*, 2018, **8**(59), 33583–33599.
23 T. Li, X. Wang, Y. Chen, J. Liang and L. Zhou, *Chem. Eng. J.*, 2020, **393**, 124735.
24 H. Xie, L. I. Jie and N. Liu, *Environ. Sci. Technol.*, 2020, 43.
25 Y. Tian, F. Liu, B. Sun, Z. Tong, P. Fu, J. Zhang, W. Bi, S. Xu and G. Pei, *J. Environ. Chem. Eng.*, 2023, 109441.
26 N. A. A. Bakar, N. A. Salleh, N. A. A. Hamid, C. A. C. Abdullah, W. Rahiman, W. J. Basirun, S. Kheawhom and A. A. Mohamad, *Mater. Today Proc.*, 2022, **60**, 1036–1041.
27 M. K. Adak, H. K. Basak, S. Kumar and B. Chakraborty, *ACS Appl. Nano Mater.*, 2024, **7**, 8329–8340.